mater.scichina.com link.springer.com

Sci China Mater 2025, 68(9): 3203–3211
https://doi.org/10.1007/s40843-025-3563-0

SPECIAL ISSUE: Celebrating the 130th Anniversary of Tianjin University

Broadband-absorbing structurally distorted cocrystal with enhanced nonradiative decay for solar interfacial water evaporation

Yi Su[1†], Zefei Zheng[2†], Lingjie Sun[1*], Wenzhe Sun[1], Yongqi Zhang[3], Huapeng Liu[4], Chenfei Yang[1], Shouzhen Li[1], Miaoyu Wang[5], Xing Chen[2], Shuaishuai Ding[1], Fangxu Yang[4] and Xiaotao Zhang[1*]

ABSTRACT **Organic cocrystals have become increasingly prevalent in a variety of research domains, owing to the simple preparation, cost-effectiveness, and highly tunable properties. Particularly, the strong charge transfer (CT) interactions in cocrystals render them promising candidates for high-efficiency photothermal conversion materials. However, the majority of reported organic photothermal cocrystals exhibit planar and rigid π-conjugated structures, which restrict molecular vibrations while simultaneously impeding non-radiative dissipation processes—ultimately hindering the enhancement of photothermal conversion performance. Herein, we design a novel non-planar photothermal NMTQ cocrystal, which shows a broadband absorption range of 220–2000 nm and high photothermal conversion efficiencies from ultraviolet (UV) to near-infrared (NIR)-II region. Quantum chemical calculations have been utilized to demonstrate that the distorted butterfly-like conformation in NMTQ is conducive to non-radiative transitions via higher non-adiabatic couplings (NACs) and lower spatial overlap integral (S_r). An interfacial solar evaporation system was constructed using NMTQ cocrystals, achieving an evaporation rate of 2.158 kg m^{-2} h^{-1} with 94.96% solar-to-vapor conversion efficiency under 1 Sun irradiation. The photothermal platform demonstrated simultaneous contaminant removal functionality, establishing a sustainable strategy for clean water production through rational photothermal material design.**

Keywords: organic cocrystal, non-planar structure, photothermal conversion, solar-water evaporation

INTRODUCTION

Organic materials have demonstrated significant potential in various fields, including optoelectronic devices, flexible electronics, and energy conversion, due to their tunable structure, ease of solution processing, scalability, cost-effectiveness, flexibility, and low weight [1–3]. In particular, organic single crystals, a specific subclass of organic functional materials, offer distinct advantages such as a highly ordered long-range structure, low defect density, and high uniformity. These properties are critical for enhancing device performance compared to amorphous or polycrystalline materials [4–7]. However, traditional single-component organic crystals are often limited by their narrow functionality and struggle to meet the demands of multi-physics field coupling in complex applications [8]. This limitation has driven researchers to focus on multi-component organic crystal systems. Cocrystal engineering, as an extension of crystal engineering, involves functionalized donor (D) and acceptor (A) molecules that recognize each other, self-assemble via non-covalent interactions, and achieve functional integration and performance breakthroughs through cooperative strategies across different constituent units, which offers new avenues for developing advanced functional materials [9–13]. Since the discovery of the conductive behavior of tetrathiofulvlene-7,7,8,8-tetracyanoquinodimethane (TTF-TCNQ) cocrystal in 1973 [14], cocrystal engineering has gained attention for its low-cost, simple preparation methods, and functional integration of "1+1 > 2". Subsequent studies have uncovered a range of properties in organic cocrystals, including metallic conductivity [15], semiconductor performance [16], and ferroelectricity [17]. Moreover, the diverse molecules, well-defined crystal structures, and adjustable crystal morphologies and molecular configurations of organic cocrystals have led to their rapid emergence in numerous scientific areas, such as ambipolar charge transport [18], nonlinear optics [19], tunable fluorescence emission [20], two-photon absorption [21], thermally activated delayed fluorescence [22], optical waveguide [23,24], room-temperature phosphorescence [25], stimulus-responsive behaviors [26,27] and photocatalysis [28].

The charge transfer (CT) interaction between module units in

[1] Institute of Molecular Aggregation Science, Key Laboratory of Organic Integrated Circuits, Ministry of Education & Tianjin Key Laboratory of Molecular Optoelectronic Sciences, Tianjin University, Tianjin 300072, China
[2] Institute of Molecular Plus, Tianjin University, Tianjin 300072, China
[3] School of Science, Tianjin University, Tianjin 300354, China
[4] School of Science, Key Laboratory of Organic Integrated Circuits, Ministry of Education & Tianjin Key Laboratory of Molecular Optoelectronic Sciences, Tianjin University, Tianjin 300072, China
[5] The International Joint Institute of Tianjin University, Key Laboratory of Organic Integrated Circuits, Ministry of Education & Tianjin Key Laboratory of Molecular Optoelectronic Sciences, Tianjin University, Tianjin 300072, China
[†] Equally contributed to this work.
[*] Corresponding author (email: sunlingjie@tju.edu.cn; zhangxt@tju.edu.cn)

the organic cocrystals significantly reduces the band gap, induces a notable redshift in the absorption spectrum, enhances aggregation-caused quenching (ACQ) effects, and promotes non-radiative transitions [29–33], which offers distinct advantages in photothermal conversion. Previously, our group first proposed the application of co-crystalline materials for near-infrared (NIR) photothermal conversion in 2018 [34], taking full advantage of their broadband absorption extended to the NIR region (ca. 300–900 nm). Recently, other research groups have developed a range of organic cocrystals with superior photothermal conversion performance by enhancing CT effects, improving light absorption, and optimizing non-radiative pathways, which have enabled applications in photothermal imaging [35], photothermal biotherapy [36], and seawater desalination [37]. However, existing organic photothermal cocrystals still face the limitation of low photothermal conversion efficiency (PCE), primarily due to constraints in non-radiative pathways. Recent advancements include regulating PCE by incorporating non-planar units to create cocrystals with twisted structures [38,39] or by increasing the number or length of vibratory groups within a single molecule [40] to enhance intramolecular vibrations. Nevertheless, the light absorption range of these materials remains limited, and improvements in PCE are modest, as excessive molecular torsion can strongly inhibit CT interactions. Therefore, designing and synthesizing organic photothermal cocrystals that balance CT interactions with strong vibrational modes represents a critical challenge in advancing this field.

Based on that, we selected *N*-methylphenothiazine (N-MPTZ) as the D featuring a classical butterfly conformation and aromaticity, and tetracyanoquinodimethane (TCNQ) as the A, successfully preparing the black N-MPTZ-TCNQ (NMTQ) rod-shaped cocrystal via simple solvent evaporation method. The introduction of the strong electron-accepting unit TCNQ induces planarization of N-MPTZ during the self-assembly process, significantly reducing the dihedral angle of the molecule. This results from the strong CT effect between the D and A, which also broadens the cocrystal's absorption spectrum to 2000 nm. However, within the NMTQ cocrystal, the N-MPTZ units retain a relatively significant dihedral angle, providing a favorable condition for heat generation via photoinduced excited vibrations, which exhibit excellent photothermal conversion efficiencies of 63.23% (365 nm), 73.91% (808 nm), and 62.51% (1550 nm). Further, an interfacial solar-driven water evaporator designed by polyurethane (PU) sponge, which shows a superfast evaporation rate of 2.158 kg m^{-2} h^{-1} and a high solar-to-vapor efficiency of 94.96%.

EXPERIMENTAL SECTION

Materials and cocrystal preparation

N-MPTZ (98%, CAS: 1207-72-3) was purchased from Shanghai Aladdin Biochemical Technology Co., Ltd. TCNQ (98%, CAS: 1518-16-7) was purchased from Shanghai TCI Co., Ltd. Acetonitrile (HPLC) was purchased from Tianjin Bohua Chemical Co., Ltd. PU sponge was purchased from Dongguan Henglitai Packaging Products Co., Ltd. All materials were directly used without further purification.

Crystal growth and characterization

The NMTQ was prepared by a solution-evaporation method. In a typical experiment, 0.05 mmol (10.7 mg) of N-MPTZ and 0.05 mmol (10.2 mg) of TCNQ were dissolved in 10 mL of acetonitrile at a molar ratio of 1:1. The solvent was then carefully evaporated to yield NMTQ. The crystal structure was obtained by X-ray diffraction (XRD) (XtaLAB Fr-X) with Cu Kα radiation (45 kV, 66 mA). Powder XRD (PXRD) patterns were tested by a Rigaku Smart Lab 9 kW with Cu Kα radiation (λ = 1.542 Å) operating at 45 kV and 200 mA.

Theoretical calculations

All quantum chemical calculations were performed using the Gaussian 09 [41] and ORCA 5.0.3 [42] software packages. Geometry optimizations of the ground state (S_0) were conducted at the B3LYP/6-311G** theoretical level, incorporating Grimme's D3 dispersion correction, with tight convergence criteria and disabling symmetry constraints. The geometries of the first excited state (S_1) were optimized using time-dependent density functional theory (TDDFT) with the CAM-B3LYP functional. Non-adiabatic coupling (NAC) vectors between S_0 and S_1 were calculated to account for internal conversion dynamics. To further elucidate the charge transfer characteristics of the excited states, hole-electron analysis was employed by Multiwfn 3.8 [43], applying an isosurface value of 0.05 a.u., along with the evaluation of transition density matrices.

Photothermal conversion property measurements

The temperature variation of the sample subjected to 365/808/1550 nm adjustable power laser irradiation was captured employing an infrared thermal imager (FLUKE Ti480 PRO), and the power density value was monitored with an optical power densimeter (CEAULIGHT, CEL-NP2000-2A).

Interfacial solar-water evaporation measurements

Water evaporation experiments were conducted under solar simulator irradiation (Enlitech, SS-F5-3A), with an irradiation density of 1 kW m^{-2} (the temperature during the water evaporation property tests was 24 °C, and the humidity was 38%). Deionized water was generated utilizing a deionization instrument (OS007XXM1). The loss of water mass was precisely recorded using an electronic balance (Sartorius BCE224-1CCN). The concentration of metal ions in both the seawater and the desalinated condensate water was determined through the use of an inductively coupled plasma optical emission spectrometer (Agilent, ICP-OES-5110).

RESULTS AND DISCUSSION

Design and preparation of NMTQ cocrystal

To investigate the electronic repulsion or attraction ability of the selected molecules, electrostatic potential (ESP) analysis was conducted on them (Fig. 1a). The red area is mainly distributed on the two benzene rings and the S atom of N-MPTZ, showing a strong electron-rich property. In contrast, TCNQ exhibits an obvious electron-deficient property. The complementary electrostatic potential energy of two units provides a good basis for the growth and preparation of CT cocrystal. Furthermore, solvent evaporation method was used to successfully prepare the NMTQ. Through CT interaction, N-MPTZ and TCNQ can recognize each other and self-assemble into black rod-shaped crystals, whose morphology exhibits a pronounced contrast with their individual units of N-MPTZ and TCNQ (Fig. 1b–d). To

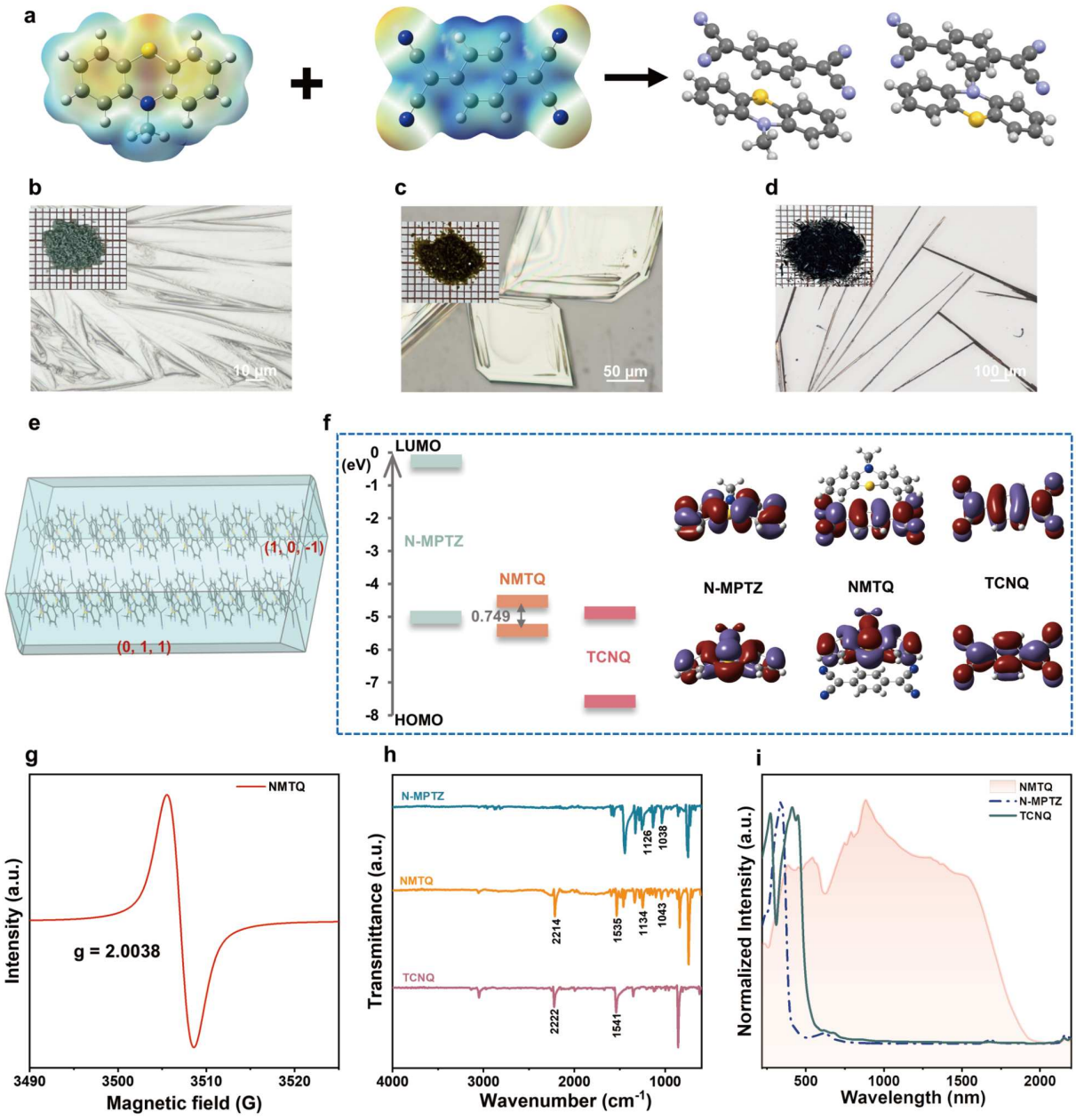

Figure 1 (a) ESP maps and co-crystallization process of N-MPTZ, TCNQ and NMTQ cocrystal (b–d) with corresponding optical microscopy images. Top left inset of the corresponding powders. (e) Molecular packing structure of the cocrystals. (f) Calculated energy level and MO diagrams (iso = 0.02) of N-MPTZ, TCNQ and NMTQ cocrystal. (g) ESR spectrum of NMTQ. (h) FTIR spectra. (i) UV-vis-NIR absorption spectra of N-MPTZ, TCNQ and NMTQ.

gain deeper insight into the intermolecular interactions and packing arrangements within the NMTQ cocrystal, we performed single-crystal XRD analyses based on a selected high-quality cocrystal. NMTQ belongs to the monoclinic $P2_1/m$ space group with cell parameters of a = 6.9129 Å, b = 13.2399 Å, c = 21.8084 Å, α = 90°, β = 91.950°, and γ = 90° (Table S1). During the co-crystallization, the π-π interactions between molecules play a non-negligible role. Fig. S1 presents that NMTQ cocrystal has mixed stacking packing modes, wherein N-MPTZ and TCNQ alternately arrange to pack with a face-to-face pattern in ···D···A···D···A··· column, which exhibits a D-A distance of 3.347 Å. Additionally, based on CrystalExplorer (CE-B3LYP functional), the calculated contribution of C···C interactions and N–H in NMTQs is 20.5% and 18.0% based on the Hirshfeld surface (Fig. S3). Moreover, the XRD pattern of the NMTQs exhibits a distinctive profile that is clearly different from those of the individual constituent monomers, as evidenced in Fig. S4. Notably, the diffraction peaks corresponding to the (011) and (10−1) planes are in excellent agreement with the exposed crystal planes observed in the simulated growth morphology depicted in Fig. 1e, thereby confirming the structural consistency. In order to find out the CT interaction and behavior of co-crystallization in NMTQ, DFT calculations were used to obtain the molecular orbital (MO) diagram and energy levels of N-MPTZ, TCNQ and NMTQ cocrystals. The frontier MO analysis reveals distinct electronic distribution characteristics in NMTQ cocrystal, as shown in Fig. 1f. The highest occupied molecular orbital (HOMO) predominantly localizes on the N-

MPTZ with an energy value of −5.348 eV, while the lowest unoccupied molecular orbital (LUMO) shows preferential distribution over the TCNQ with an energy value of −4.599 eV. Further, a remarkable bandgap reduction is observed upon co-crystallization (0.749 eV), contrasting sharply with the wide bandgaps of individual components, which originates from strong interfacial CT interaction between N-MPTZ and TCNQ.

CT interaction and photothermal properties of NMTQ

To more effectively elucidate the co-assembly process in NMTQ, a variety of characterizations were used to prove the CT interaction between N-MPTZ and TCNQ in the cocrystal. As described in Fig. 1g, electron spin resonance (ESR) exhibits strong CT interaction in the NMTQ cocrystal, where it shows a signal peak (g = 2.0038) corresponding to the presence of unpaired electrons in NMTQ. For a complete understanding of the degree of charge transfer (DCT) in NMTQ [44], we have obtained the DCT value of the NMTQs to be 0.322 based on the wavenumber variation of the C≡N stretching frequency observed in Fourier transform infrared (FTIR) measurements (Fig. 1h and Table S2). Furthermore, the Raman analysis revealed distinct vibrational shifts associated with cocrystal self-

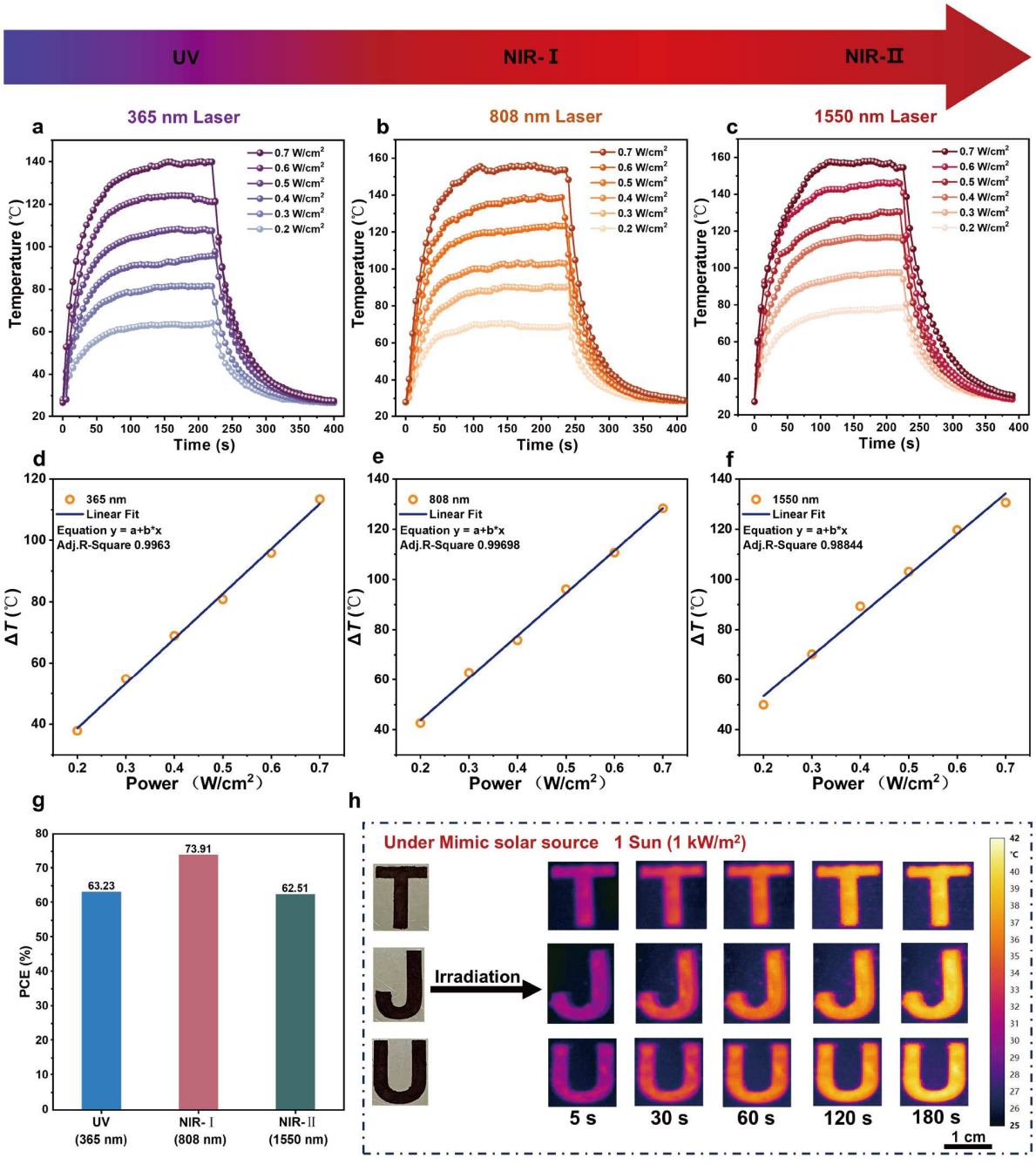

Figure 2 Temperature variations of NMTQ cocrystals with different power densities under (a) 365 nm, (b) 808 nm and (c) 1550 nm laser irradiation. Linear relationship between ΔT and the different power densities under (d) 365 nm, (e) 808 nm and (f) 1550 nm laser irradiation. (g) Photothermal conversion efficiencies of NMTQ in different regions. (h) Thermal pattern images of NMTQs under 1 Sun illumination.

assembly (Fig. S5). The characteristic C=C stretching vibration of TCNQ at 1452 cm^{-1} was shifted to 1441.6 cm^{-1} in NMTQs, indicative of electron density redistribution through π-π interactions. Concomitantly, the symmetric stretching modes of N-MPTZ exhibited significant red shifts: the Ph–N–Ph vibration at 1258 cm^{-1} red-shifted to 1273.5 cm^{-1}, while the Ph–S–Ph vibration at 696.6 cm^{-1} moved to 708.2 cm^{-1}. These systematic low-frequency displacements of D and A vibrational signatures collectively demonstrate substantial CT interactions between the constituent molecules, confirming the establishment of strong D-A coupling in the co-crystalline architecture. Fig. 1i illustrates the ultraviolet-visible-near infrared (UV-vis-NIR) absorption spectra of N-MPTZ, TCNQ and NMTQ. Notably, the formation of CT cocrystal NMTQ induces remarkable broadband optical absorption spanning 220–2000 nm, which extends across the UV to NIR-II region.

The wide absorption of NMTQs enabled efficient photothermal conversion across multiple spectral windows. To evaluate this property, laser irradiation at 365 nm (UV), 808 nm (NIR-I), and 1550 nm (NIR-II) was employed, as these wavelengths correspond to the classical absorption bands of each respective region. Based on that, NMTQs exhibited remarkable wavelength-independent heating performance, as demonstrated in Fig. 2a–c, achieving equilibrium temperatures of 139.9, 156.1, and 157.9 °C under 0.7 W cm^{-2} irradiation, respectively. Through the cooling curves and linear regression analysis of lnθ versus time, the photothermal conversion efficiencies were calculated as 63.23% (365 nm), 73.91% (808 nm), and 62.51% (1550 nm) (Fig. 2g, Figs S6 and S7), surpassing most reported organic photothermal agents in comparable spectral regions (Table S3). Interestingly, NMTQs can also demonstrate excellent optical power dependence, meaning that under different power irradiation (0.2–0.7 W cm^{-2}), the maximum temperature increments show a linear dependence with the power of irradiation (Fig. 2d–f). To intuitively validate the broadband photothermal capability of NMTQ cocrystals, we conducted "TJU" thermal imaging based on NMTQ powders under simulated sunlight (AM 1.5). The infrared thermal imaging data (Fig. 2h) revealed that NMTQ samples attained an equilibrium temperature of ~41 °C within 180 s under 1 Sun illumination.

Photothermal mechanism of NMTQ

The superior PCE of NMTQ originates from the complete suppression of radiative transitions during the co-crystallization of N-MPTZ and TCNQ. As shown in Fig. S8, the solid-state fluorescence spectroscopy revealed complete emission quenching upon co-crystallization, while the NMTQ cocrystals showed no photon emission compared with N-MPTZ and TCNQ, indicating that the effective non-radiative pathways are coupled after co-crystallization. The heat energy generation in the excited state is predominantly attributed to the enhancement of non-radiation pathways. In the NMTQ cocrystal, N-MPTZ has a butterfly-like non-planar geometry, which has a dihedral angle of 36.34° (Fig. S9a). During the co-crystallization with TCNQ, the molecules retain a relatively large curvature, although they tend to flatten due to CT interactions (Fig. S9b). In order to demonstrate the contribution of the non-planar structure to the non-radiative channel, a fully planar An-TCNQ cocrystal was successfully assembled with TCNQ using planar molecular anthracene as the D (Fig. 3a). Under different laser irradiation, the maximum temperature increments of both cocrystals can be

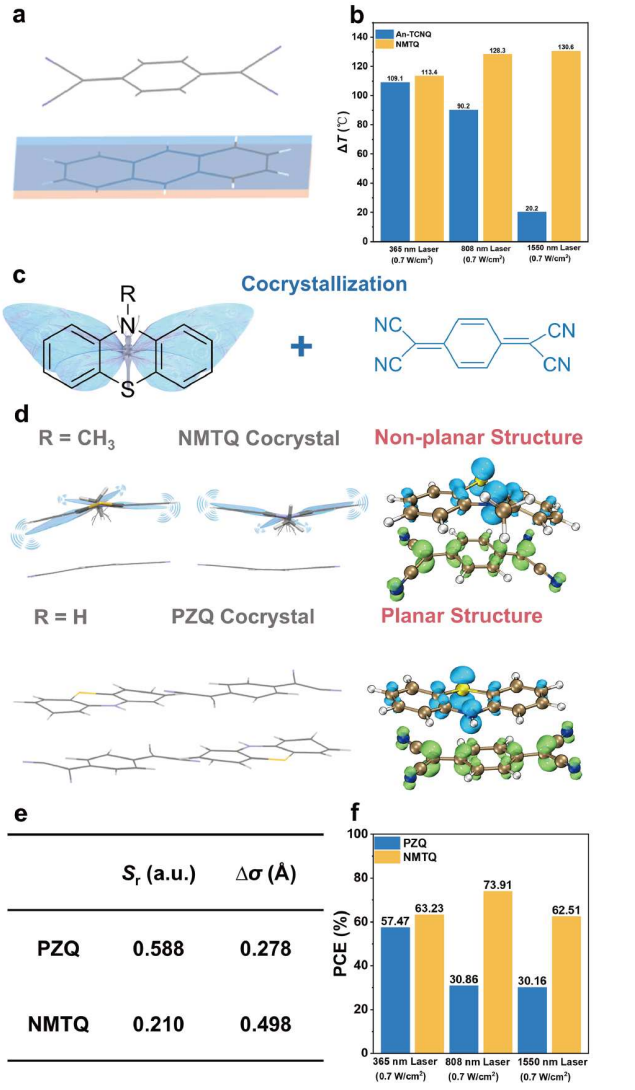

Figure 3 (a) Stacking model of An-TCNQ. (b) Differences in heating between An-TCNQ and NMTQ. (c) Co-assembly model with TCNQ based on phenothiazine donors. (d) Crystal stacking of NMTQ and PZQ and the corresponding hole-electron analysis of excited states. (e) Spatial overlap integral (S_r) and the centroid separation distance ($\Delta\sigma$) of NMTQ and PZQ. (f) Comparison of PCE between NMTQ and PZQ at 365, 808, and 1550 nm lasers.

seen in Fig. 3b, NMTQs demonstrate superior heating efficiency, especially in the NIR region.

To elucidate the potential mechanism by which non-planar structures enhance the performance of photothermal conversion, the norms of NACs between S_0 and S_1 for planar structured An-TCNQ and non-planar NMTQ have been systematically calculated [45,46]. As summarized in Table S4, the significantly higher NAC norm observed for non-planar NMTQ (1.3988) compared to planar An-TCNQ (0.5088) suggests that NMTQ cocrystal exhibits a greater degree of non-radiative index, which can be attributed to the non-planar structures in NMTQ (Table S4). However, the substantial molecular disparities, particularly the occurrence of heteroatoms such as S and N in NMTQ, could potentially contribute to the intensification of non-radiation. Moreover, the reason for the persistence of a specific bending

configuration in the NMTQ cocrystal has not yet been clarified. Based on that, phenothiazine (PTZ) was utilized as a D, which, as an unmodified by methyl substitution structure, engineered PTZ-TCNQ (PZQ) assemblies while preserving PTZ's butterfly conformation. Surprisingly, as shown in Fig. 3c and Fig. S10, structural analyses reveal distinct packing patterns modulated by alkyl chain substituents: methyl steric hindrance in NMTQ restricts molecular planarization (dihedral angle: 36.34°→14.40°), whereas reduced steric effects in PZQ enable near-planar configurations (21.55°→3.47°). The observed discrepancy can be attributed to the presence of methyl groups, which introduce spatial site resistance and significantly contribute to the maintenance of the bent conformation of non-planar molecules during cocrystal formation. Photothermal performance (Fig. 3f and Figs S11–S13) demonstrates that excited-state heat generation primarily stems from intermolecular vibrational dissipation. Notably, the hole-electron distribution characteristics of PZQ and NMTQ exhibit marked differences in Fig. 3e. In the first excited state, methyl-substituted NMTQ demonstrates a substantially lower spatial overlap integral (S_r = 0.210) than PZQ (S_r = 0.588), implying reduced localization of electron-hole pairs in NMTQ. Further, the increased centroid separation distance ($\Delta\sigma$) between hole and electron densities in NMTQ (0.498 Å) relative to PZQ (0.278 Å) suggests weaker Coulombic attraction, facilitating vibrational energy dissipation from the excited state (Fig. 3d). These comparative hole-electron analyses clearly demonstrate that the introduction of methyl groups with higher steric hindrance in NMTQ induces a more distorted butterfly-like conformation compared to PZQ. This structural distortion enhances charge separation and reduces exciton binding energy, synergistically favoring non-radiative transitions and ultimately improving photothermal conversion performance.

The findings underscore the critical role of substituent-induced conformational control in optimizing non-radiative pathways for advanced photothermal materials. In summary, the non-planar architecture of NMTQ has been demonstrated to exhibit excellent photothermal conversion performance due to its non-planar structure and the presence of methyl groups, which underscores the critical role of substituent-induced conformational control in optimizing non-radiative pathways in photothermal materials.

NMTQ-based solar-water evaporation system

NMTQ demonstrates exceptional solar energy utilization through broadband spectral harvesting and high photothermal conversion performance, positioning it as a promising material platform for interfacial solar-driven desalination and water purification technologies. Considering economy and convenience, PU sponge was selected as the evaporator skeleton. Meanwhile, the hierarchically porous architecture of PU sponge not only synergistically augments photon harvesting through multi-scale light scattering but also can establish interconnected hydraulic pathways for efficient interfacial water transport during evaporation. We employed the *in-situ* method to facilitate the nucleation and co-crystallization of NMTQ within the voids of blank PU sponges (Fig. S14). As depicted in Fig. 4a and Fig. S15, the initially smooth voids of the pristine PU sponge transformed into a roughened surface following the NMTQ loading, providing compelling evidence that NMTQ indeed successfully grew *in situ* within the evaporator. The diffraction peaks corresponding to NMTQ-crystals observed in the PXRD results of NMTQ-PU further confirm the successful growth and incorporation of NMTQ into the voids of blank PU sponges (Fig. S16). We loaded 0–30 mg of NMTQ samples respectively in the PU sponge, under the solar irradiation of 1 kW m^{-2}, the NMTQ-PUs present a higher steady-state temperature over blank PU (Fig. 4b, Fig. S17). To more precisely determine the optimal loading of NMTQ cocrystals in PU sponge, water evaporation experiments were performed on sponges with varying NMTQs loaded under identical environmental conditions. As shown in Fig. 4c, the amount of water evaporation increases gradually with the increase of the amount of loaded NMTQ samples according to the mass reduction of water over time.

The calculated water evaporation rates for PU, NMTQ-PU-5 mg, NMTQ-PU-10 mg, NMTQ-PU-20 mg, and NMTQ-PU-30 mg are 1.203, 1.589, 1.784, 2.158 and 1.796 kg m^{-2} h^{-1} with corresponding solar water conversion efficiencies (η) of 33.80%, 66.43%, 82.54%, 94.96% and 66.59%, respectively. Based on that, NMTQ-PU-20 mg was selected as the best evaporation system. Moreover, as exhibited in Fig. S18, following 6 cycles for 6 h, the evaporator consistently maintains a robust water evaporation rate, which demonstrates the potential for the long-term application of this evaporation system.

Additionally, to validate the high-performance water purification capability of the NMTQs-based evaporation system, water purification experiments were systematically conducted. As schematically illustrated in Fig. 4d, the clean water generation and collection model demonstrates that the NMTQ-PU evaporator enables rapid production of the purified water vapor under simulated solar irradiation, and the generated vapor subsequently undergoes condensation processes, yielding ultrapure water with negligible impurity content. First, rhodamine B (RhB) aqueous solution (100 ppm) was employed as a representative model for dye wastewater. As evidenced in Fig. 4e, during the solar evaporation treatment, the coloration of RhB solution was eliminated completely, corresponding with yielding a visually transparent liquid. UV-vis-NIR spectroscopic analysis confirmed the complete disappearance of characteristic RhB absorption peaks at 554 nm, demonstrating an effective wastewater purification results can be achieved through the interface solar evaporation process. Further, Bohai water was used as the feed source. The concentration of metal ions (Na^+, Mg^{2+}, Ca^{2+}, and K^+) in both the original seawater and the desalinated condensate was measured using inductively coupled plasma optical emission spectrometry (ICP-OES). Results show a significant reduction in metal ion concentration in the desalinated condensate compared to the original seawater (Fig. 4f). Additionally, the salinity of the evaporated water complies with the World Health Organization (WHO) standards for drinking water.

CONCLUSIONS

In this work, the NMTQ cocrystal was synthesized via strong CT interactions. Single-crystal analysis and DFT calculations revealed the existence of π-π interactions, a narrowed bandgap (0.749 eV), and broadband absorption. Additionally, NMTQ demonstrates outstanding photothermal conversion efficiencies of 63.23%, 73.91%, and 62.51% under 365, 808, and 1550 nm lasers, respectively. The non-planar geometry and methyl-induced steric effects in NMTQ suppressed radiative transitions by reducing electron-hole overlap and enhancing charge separation, as validated by comparative NAC norms and struc-

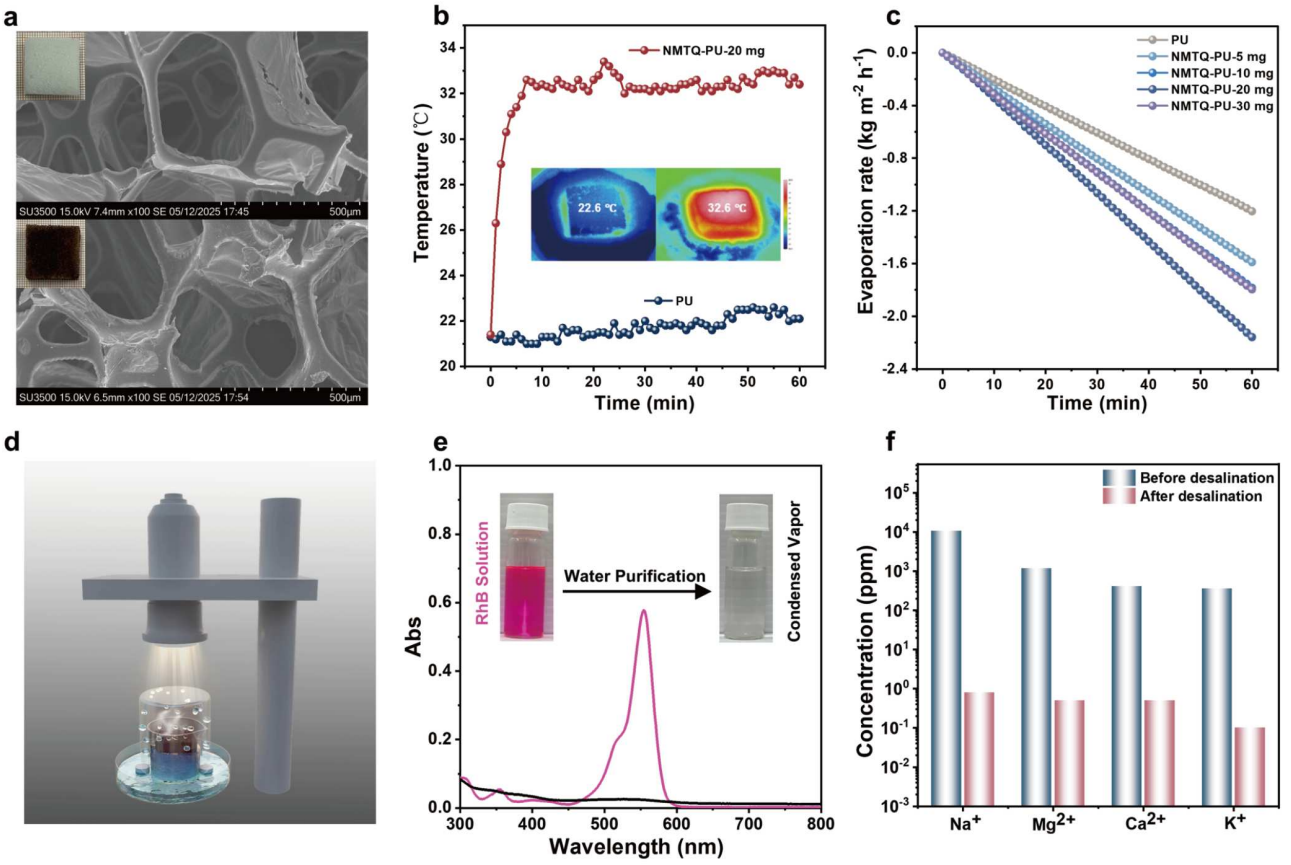

Figure 4 (a) SEM images of PU and NMTQ-PU. Top left of the corresponding optical images. (b) Surface temperature changes of the blank PU and 20 mg NMTQ loaded PU under 1 Sun irradiation and the IR thermal images inset shows. (c) Mass changes of the blank PU and different loaded NMTQ samples in the evaporation system within 1 h under 1 Sun illumination. (d) Clean water generation and collection model based on NMTQ cocrystals. (e) UV-vis-NIR absorption spectra of water contaminated with RhB, both before (pink line) and after (black line) purification. Photographs of the samples are displayed in the inset. (f) Ion concentration levels in seawater before (blue) and after (red) solar desalination.

tural analogs. Based on the superior photothermal performance of NMTQ cocrystal, a PU sponge-based evaporation system was designed, which demonstrated a water evaporation rate of 2.158 kg m^{-2} h^{-1} and a water evaporation efficiency of up to 94.96% under 1 Sun irradiation. More importantly, this solar-water evaporation system has shown effective performance in purifying dye-contaminated water and desalinating seawater. This study establishes the molecular conformation engineering as a pivotal strategy for optimizing non-radiative decay in advanced photothermal materials, offering scalable solutions for sustainable solar-driven water purification.

Received 24 May 2025; accepted 11 July 2025; published online 30 July 2025

1 Wang C, Dong H, Hu W, *et al.* Semiconducting π-conjugated systems in field-effect transistors: a material odyssey of organic electronics. Chem Rev, 2012, 112: 2208–2267
2 Wang H, Sun Q, Yang F, *et al.* Ultrahigh resolution X-ray imaging with thin-film scintillators based on aggregation-induced delayed fluorescence luminogens. SmartMat, 2025, 6: e70002
3 Zhu Y, Xu Z, Wu F, *et al.* Liquid-crystal elastomers based on covalent adaptable networks: from molecular design to applications. Sci China Mater, 2023, 66: 3004–3021
4 Sun Y, Hu W. Novel machine learning framework for thermal conductivity prediction by crystal graph convolution embedded ensemble. SmartMat, 2022, 3: 474–481
5 Yang F, Sun L, Duan Q, *et al.* Vertical-organic-nanocrystal-arrays for crossbar memristors with tuning switching dynamics toward neuromorphic computing. SmartMat, 2021, 2: 99–108
6 Ye G, Li S, Ding R, *et al.* Unveiling the interfacial properties of organic single-crystal hole-transporting layers for high-performance light-emitting devices. SmartMat, 2025, 6: e1329
7 Fu B, Sun L, Liu L, *et al.* Low-power high-mobility organic single-crystal field-effect transistor. Sci China Mater, 2022, 65: 2779–2785
8 Zhou K, Dong H, Zhang H, *et al.* High performance n-type and ambipolar small organic semiconductors for organic thin film transistors. Phys Chem Chem Phys, 2014, 16: 22448–22457
9 Sun L, Wang Y, Yang F, *et al.* Cocrystal engineering: a collaborative strategy toward functional materials. Adv Mater, 2019, 31: 1902328
10 Wang Y, Yang J, Gong Y, *et al.* Host-guest materials with room temperature phosphorescence: tunable emission color and thermal printing patterns. SmartMat, 2020, 1: e1006
11 Sun L, Zhu W, Zhang X, *et al.* Creating organic functional materials beyond chemical bond synthesis by organic cocrystal engineering. J Am Chem Soc, 2021, 143: 19243–19256
12 Wang X, Wang Z, Wang X, *et al.* Recent advances of organic cocrystals in emerging cutting-edge properties and applications. Angew Chem Int Ed, 2024, 63: e202416181
13 Wang W, Luo L, Sheng P, *et al.* Multifunctional features of organic charge-transfer complexes: advances and perspectives. Chem Eur J, 2021, 27: 464–490
14 Coleman LB, Cohen MJ, Sandman DJ, *et al.* Superconducting fluctuations and the peierls instability in an organic solid. Solid State Commun, 1973, 12: 1125–1132
15 Mahns B, Kataeva O, Islamov D, *et al.* Crystal growth, structure, and

transport properties of the charge-transfer salt picene/2,3,5,6-tetrafluoro-7,7,8,8-tetracyanoquinodimethane. Cryst Growth Des, 2014, 14: 1338–1346
16 Li T, Fu S, Ding S, *et al.* Advancing room-temperature magnetic semiconductors with organic radical charge transfer cocrystals. Adv Mater, 2025, 37: 2414719
17 Zhang C, Wang X, Li Y, *et al.* Spin in organic cocrystals. Chem Eur J, 2023, 29: e202300481
18 Li S, Zheng L, Chan Y, *et al.* An organic cocrystal based on phthalocyanine with ideal packing mode towards high-performance ambipolar property. J Mater Chem C, 2022, 10: 9596–9601
19 Zhu W, Zhu L, Sun L, *et al.* Uncovering the intramolecular emission and tuning the nonlinear optical properties of organic materials by cocrystallization. Angew Chem Int Ed, 2016, 55: 14023–14027
20 Ye H, Liu G, Liu S, *et al.* Molecular-barrier-enhanced aromatic fluorophores in cocrystals with unity quantum efficiency. Angew Chem Int Ed, 2018, 57: 1928–1932
21 Sun L, Zhu W, Wang W, *et al.* Intermolecular charge-transfer interactions facilitate two-photon absorption in styrylpyridine-tetracyanobenzene cocrystals. Angew Chem Int Ed, 2017, 56: 7831–7835
22 Sun L, Hua W, Liu Y, *et al.* Thermally activated delayed fluorescence in an organic cocrystal: narrowing the singlet-triplet energy gap via charge transfer. Angew Chem Int Ed, 2019, 58: 11311–11316
23 Lv Q, Wang XD, Yu Y, *et al.* Selective epitaxial growth of organic heterostructure via cocrystal engineering: towards oriented signal conversion. Sci China Mater, 2023, 66: 3968–3976
24 Zhuo M, Yuan Y, Su Y, *et al.* Segregated array tailoring charge-transfer degree of organic cocrystal for the efficient near-infrared emission beyond 760 nm. Adv Mater, 2022, 34: 2107169
25 Yang C, Fu S, Li S, *et al.* A chiral cocrystal strategy producing room-temperature phosphorescence and enhancing circularly polarized luminescence. Adv Opt Mater, 2025, 13: 2402522
26 Zhang Y, Wu H, Sun Y, *et al.* Cocrystal engineering: tuning the charge transfer excitons for highly sensitive luminescent switching materials under multiple stimuli. Sci China Mater, 2022, 65: 1320–1328
27 Ye Y, Qi L, Sun Y, *et al.* Integrating dual photoresponsive molecules via a cocrystal strategy: photosalient effects, negative photochromism, and fluorescence enhancement. Sci China Mater, 2024, 67: 223–231
28 Wang L, Deng J, Jiang M, *et al.* Arene-perfluoroarene interactions in molecular cocrystals for enhanced photocatalytic activity. J Mater Chem A, 2023, 11: 11235–11244
29 Fu S, He D, Zhang X. Photothermal conversion mechanism of the dibenzotetrathiafulvalene-tetracyanobenzene cocrystal based on the transitions between the ground and excited states. Sci China Mater, 2024, 67: 242–250
30 Zhao L, Ren X, Yan X. Assembly induced super-large red-shifted absorption: the burgeoning field of organic near-infrared materials. CCS Chem, 2021, 3: 678–693
31 Liang W, He S, Wu S. Fluorescence imaging in second near-infrared window: developments, challenges, and opportunities. Adv Nano-Biomed Res, 2022, 2: 2200087
32 Zhang H, Xu X, Cao Y, *et al.* Unlocking the power of photothermal agents: a universal platform for smart immune NIR-agonists for precise cancer therapy. Angew Chem Int Ed, 2025, 64: e202424830
33 Wang C, Zhong W, Sun X, *et al.* NIR-activable charge transfer agents for synergistic photoimmunotherapy. Angew Chem Int Ed, 2025, 64: e202416828
34 Wang Y, Zhu W, Du W, *et al.* Cocrystals strategy towards materials for near-infrared photothermal conversion and imaging. Angew Chem Int Ed, 2018, 57: 3963–3967
35 Zhao YD, Han J, Chen Y, *et al.* Organic charge-transfer cocrystals toward large-area nanofiber membrane for photothermal conversion and imaging. ACS Nano, 2022, 16: 15000–15007
36 Lim AJ, Littlefield KP, Alkalani Z, *et al.* Synergistic cancer photoimmunotherapy by harnessing near-infrared-activated nanoparticles containing charge transfer complexes. Angew Chem Int Ed, 2025, 64: e202423550
37 Liu J, Li T, Yu H, *et al.* Integrating molecular motions in ternary cocrystals for NIR-II photothermal conversion. Angew Chem Int Ed, 2025, 64: e202413805
38 Cao H, Gao Y, Wu B, *et al.* Tuning molecular packing by twisting structure to facilely construct highly efficient solid-state fluorophores for two-photon bioimaging and photodynamic therapy. Adv Funct Mater, 2024, 34: 2315692
39 Li T, Liu BT, Liu JC, *et al.* Near-infrared emission in organic cocrystals based on twisted-component pseudoencapsulation. ACS Mater Lett, 2025, 7: 2246–2254
40 Chen YT, Wen X, He J, *et al.* Boosting near-infrared photothermal conversion by intermolecular interactions in isomeric cocrystals. ACS Appl Mater Interfaces, 2022, 14: 28781–28791
41 Frisch MJ, Trucks GW, Schlegel HB, *et al.* Gaussian 09. Revision A.1. Wallingford, CT: Gaussian, Inc. 2009
42 Neese F. The ORCA program system. WIREs Comput Mol Sci, 2012, 2: 73–78
43 Lu T, Chen F. Multiwfn: a multifunctional wavefunction analyzer. J Comput Chem, 2012, 33: 580–592
44 Hu P, Du K, Wei F, *et al.* Crystal growth, HOMO-LUMO engineering, and charge transfer degree in perylene-F_xTCNQ (x = 1, 2, 4) organic charge transfer binary compounds. Cryst Growth Des, 2016, 16: 3019–3027
45 Acharya S, Bhattacharjee D, Sarkar J, *et al.* Spectroscopic study of non-amphiphilic 2-(4-biphenylyl)-5-(4-*tert*-butylphenyl)-l,3,4-oxadiazole aggregates at air-water interface and in Langmuir-Blodgett films. Chem Phys Lett, 2004, 393: 1–6
46 Pritchard BP, Altarawy D, Didier B, *et al.* New basis set exchange: an open, up-to-date resource for the molecular sciences community. J Chem Inf Model, 2019, 59: 4814–4820

Acknowledgement This work was financially supported by the National Key Research and Development Program of China (2022YFA1204401) and the National Natural Science Foundation of China (52403301, 52373194, 52473239, 52121002, U21A6002 and U24A20293).

Author contributions Sun L and Zhang X conceived and supervised this study; Su Y and Zheng Z wrote the paper; Ding S and Yang F contributed to the revision of this paper; Chen X and Zheng Z performed theoretical calculations; Su Y and Sun W performed most of the experiments including the material preparation and characterization; Zhang Y and Li S contributed the photothermal conversion measurement; Liu H, Wang M, and Yang C contributed the crystallographic analysis. All authors contributed to discussion and manuscript review.

Conflict of interest The authors declare that they have no conflict of interest.

Supplementary information Supplementary materials are available in the online version of the paper.

Yi Su is a doctoral student at Institute of Molecular Aggregation Science, Key Laboratory of Organic Integrated Circuits, Ministry of Education & Tianjin Key Laboratory of Molecular Optoelectronic Science, Tianjin University. Her current research focuses on the design of organic cocrystals and innovative interfacial water evaporation devices.

Zefei Zheng is a Master's student at Institute of Molecular Plus, Tianjin University. His current research focuses on the application of machine learning techniques to predict molecular polarizability.

Lingjie Sun is an associate professor at Tianjin University. She received her PhD degree from the Department of Chemistry, School of Science, Tianjin University in 2020 with the supervisor of Prof. Wenping Hu. Her research interests focus on the design, characterization, and optoelectronic properties of organic cocrystals.

Xiaotao Zhang is a professor at Tianjin University. He received his PhD degree from the Institute of Chemistry, Chinese Academy of Sciences, in 2012 after he got his MSc degree (2007) at Zhejiang University. His research interests include the design and synthesis of novel organic semiconductors, the fabrication and characterization of organic optoelectronic devices.

具有增强非辐射跃迁结构变形的宽带吸收有机共晶用于太阳能界面水蒸发

苏易[1†], 郑泽飞[2†], 孙玲杰[1*], 孙文哲[1], 张永琦[3], 刘华鹏[4], 杨晨飞[1], 李守真[1], 王淼宇[5], 陈星[2], 丁帅帅[1], 杨方旭[4], 张小涛[1*]

摘要 有机共晶体具有制备简单、价格低廉和高度可调的特性，广泛应用于各研究领域. 特别地，强烈的电荷转移相互作用使共晶成为新型的高效光热转换材料. 然而，大多数已报道的有机光热共晶体都表现出平面和刚性π-共轭结构，这限制了非辐射耗散过程从而限制光热转换性能的提高. 在此，我们设计了一种新型非平面光热NMTQ共晶，其具有220–2000 nm的宽带吸收范围，在紫外至近红外II区具有很高的光热转换效率. 量子化学计算证明，NMTQ的扭曲蝴蝶状构象有利于通过更高的非绝热耦合和更低的空间重叠积分实现非辐射转变. 利用NMTQ共晶体构建了一个界面太阳能蒸发系统，实现了2.158 kg m^{-2} h^{-1}的蒸发率和94.96%的太阳能-蒸汽转换效率. 同时展示了可持续的清洁水生产效果.